J Mater Sci: Mater Electron (2025) 36:1004

Insights into the Structural, Microstructural and Thermoelectric Properties of Ce/Cr co-doped $CaMnO_3$ manganites

L. Korkmaz[1], C. Özçelik[2], M. Gürsul[1], M. A. Torres[2], M. A. Madre[2], A. Sotelo[2], and B. Özçelik[1,*]

[1] *Department of Physics, Faculty of Sciences and Letters, Çukurova University, 01330 Adana, Turkey*
[2] *INMA (CSIC-Universidad de Zaragoza), Maria de Luna, 50018 Saragossa, Spain*

Received: 18 March 2025
Accepted: 31 May 2025

ABSTRACT

This study investigates the structural, microstructural, and thermoelectric properties of Cr-substituted $Ca_{0.99}Ce_{0.01}Mn_{1-x}Cr_xO_3$ materials synthesized via solid-state reaction method. X-ray diffraction (*XRD*) analysis confirms the single-phase orthorhombic structure (*Pnma* space group) for all compositions, with successful incorporation of Cr into the crystal structure. A slight decrease in lattice parameters is observed, attributed to the smaller ionic radius of Cr^{3+} compared to Mn^{3+}. Field Emission scanning electron microscope (FESEM) reveals that Cr doping inhibits grain growth and induces crack formation, which significantly impacts electrical resistivity. The charge transport mechanism is well-described by Mott's adiabatic small polaron model, with activation energy increasing with Cr doping. The Seebeck coefficient remains negative across all temperatures, indicating n-type conduction, and the highest power factor (~0.35 mW/K^2m) is achieved for the 0.03Cr-doped sample at 800 °C. These results highlight the potential of Cr-doped $CaMnO_3$ as a cost-effective and scalable thermoelectric material, with performance comparable to that reported using more complex synthesis methods.

1 Introduction

The rising global energy demand is a major concern, driven by the depletion of natural resources and the adverse environmental effects of pollution and global warming. Greenhouse gases are emitted worldwide, largely driven by increasing energy needs for transportation, heating, cooling, and air conditioning. These issues have prompted researchers to explore alternative and sustainable energy harvesting solutions technologies that address this rising energy demand. A particularly eco-friendly and straightforward approach involves converting waste heat or ambient environmental heat into usable energy. Green energy technologies have made substantial contributions to mitigating the energy and environmental challenges posed by modern technological demands. While these technologies offer undeniable benefits through clean energy production, which help reducing environmental issues to some extent, greenhouse gas emissions, associated with their large-scale production, cannot

Address correspondence to E-mail: ozcelik@cu.edu.tr

https://doi.org/10.1007/s10854-025-15116-z
Published online: 12 June 2025

be overlooked. Therefore, improving the efficiency of these technologies is essential.

A promising strategy for improving energy system efficiency is the use of waste heat recovery techniques. In this context, thermoelectric materials, which can directly convert waste heat into electricity, play a key role in driving sustainable energy advancements [1, 2]. By combining appropriate p- and n-type thermoelectric materials, functional modules have been developed for both power generation and cooling applications [3–6]. Thermoelectric generators are valued for their dependability, self-sustaining operation, quietness, and lack of harmful emissions, making them well-suited for applications requiring durability and long operational lifespans under extreme conditions.

The efficiency of energy conversion in thermoelectric materials is commonly evaluated using the dimensionless figure of merit, $ZT = S^2T/\rho\kappa$, where S represents the Seebeck coefficient, ϱ denotes electrical resistivity, κ signifies thermal conductivity, and T is the absolute temperature. [7, 8]. The term S^2/ϱ, referred to as the power factor (PF), is linked to the electrical properties of the material. To attain a high figure of merit (ZT > 1), it is crucial to achieve a large Seebeck coefficient while minimizing both thermal conductivity and electrical resistivity. However, these parameters are interrelated, making it challenging to enhance them independently to boost their thermoelectric performance [9]. Consequently, several strategies have been implemented to enhance the ZT value, including elemental doping, advanced fabrication techniques, nanostructuring, and band engineering.

In this regard, several types of thermoelectric compounds have been considered, as GeSn alloys [10], GePb [11], PbTe [12], or $CaMnO_3$ [13]. In spite of the relatively low performances of thermoelectric oxides, they are regarded as very promising due to their advantages, as compared with the other families, as their high thermal stability, abundance in the Earth crust, and lower costs [14–16], which explain the high number of works centered on the increase of their thermoelectric performances.

On the other hand, when considering the development of efficient thermoelectric devices, high-performance p-type materials must be complemented by n-type materials with comparable properties. However, current n-type materials generally exhibit lower thermoelectric performance than their p-type counterparts [17]. As a result, considerable research efforts have been directed towards enhancing the thermoelectric properties of n-type oxide materials [9, 18–23]. Among various n-type thermoelectric materials, $CaMnO_3$ has demonstrated relatively high thermoelectric performance, particularly when subjected to targeted modifications. Elemental substitution has emerged as a promising approach for enhancing the figure of merit, ZT [9, 13, 18–25]. Doping can be introduced at two distinct cationic sites within the unit cell; the Mn site [18] or the Ca site [9, 19–21]. Notably, substituting Ca tends to yield greater improvements in thermoelectric performance than substituting Mn [18]. Replacing Ca^{2+} with trivalent or tetravalent cations has been found to enhance carrier concentration, leading to a substantial reduction in electrical resistivity, though it also results in a slight decrease in the Seebeck coefficient [9, 19, 20].

Pure $CaMnO_3$ adopts an orthorhombic perovskite structure of the $GdFeO_3$ type, classified under the *Pnma* space group. It displays an antiferromagnetic (AFM) phase with a Néel temperature (T_n) of around 125 K [26, 27]. In this arrangement, the Mn ion magnetic moments are oriented antiparallel to those of their adjacent neighbours, with superexchange interactions between Mn^{4+} ions mediated by oxygen anions, resulting in a G-type AFM configuration [28]. While $CaMnO_3$ ceramics exhibit a high Seebeck coefficient, their figure of merit (ZT) remains low at elevated temperatures due to high electrical resistivity resulting from a low charge carrier concentration. Doping the $CaMnO_3$ lattice with trivalent or tetravalent elements induces the partial reduction of Mn^{4+}–Mn^{3+} to preserve charge neutrality [29] and promotes ferromagnetic properties by enabling electron transfer from Mn^{3+} to Mn^{4+} sites, which facilitates Mn^{3+}–O–Mn^{4+} double-exchange interactions [30]. Consequently, these dopants enhance the thermoelectric properties of $CaMnO_3$ materials, making perovskite manganites promising candidates for n-type thermoelectric applications. Therefore, extensive research has been conducted to optimize their thermoelectric performance through doping modifications. Previous works have shown that Ca substitution by trivalent cations together with high oxidation metallic cations substituting Mn have shown that it is useful to enhance thermoelectric performances of $CaMnO_3$ [22]. Nevertheless, the use of trivalent cations as Mn substitutes has not been evaluated in conjunction with the Ca substitution with a higher oxidation cation.

Building on these insights, this study focuses on synthesizing co-doped $Ca_{0.99}Ce_{0.01}Mn_{1-x}Cr_xO_3$

materials ($x = 0$, 0.01, 0.03, 0.05, and 0.10) using the conventional solid-state method. As previously indicated, Ce^{4+} is substituting Ca^{2+} and should increase the Mn^{3+}/Mn^{4+} proportion to maintain charge neutrality. However, Cr^{3+} should mainly substitute Mn^{3+} due to their relatively close ionic radii [31] and, consequently, decreasing the Mn^{3+}/Mn^{4+} proportion. As a result, the objective of this work is exploring the effect of these substitutions with opposite effects on the structure and microstructure of these compounds, being correlated with their thermoelectric properties. Furthermore, these properties will be evaluated and compared with existing literature data.

2 Experimental

The $Ca_{0.99}Ce_{0.01}Mn_{1-x}Cr_xO_3$ materials ($x = 0$, 0.01, 0.03, 0.05, and 0.10) investigated in this study were synthesized using commercially available powders: $CaCO_3$ (≥ 99%, Aldrich), CeO_2 (99.995%, Aldrich), Mn_2O_3 (99%, Aldrich), and Cr_2O_3 (99.9%, Aldrich). The precursors were accurately weighed in stoichiometric ratios, thoroughly mixed, and then ball-milled at 300 rpm for 30 min using agate balls and water as the milling medium. The resulting suspensions were dried under infrared radiation, and the obtained powder underwent a two-step calcination process at 950 °C and 1050 °C for 12 h, with an intermediate manual milling step. Following calcination, a concentrated polyvinyl alcohol (PVA) solution was added to the powder to ensure uniform distribution, followed by manual milling. The dried mixture was then uniaxially pressed into pellets ($3 \times 3 \times 14$ mm^3) at approximately 400 MPa and subsequently sintered at 1310 °C for 12 h, followed by furnace cooling.

The phase composition of the sintered materials was analyzed using Rigaku Ru300 X-ray diffraction (XRD) utilizing a copper anticathode ($\lambda = 1.5406$ Å) and a scanning range of $2\theta = 15$–60°. Microstructural analyses of the samples' surfaces were performed using a field emission scanning electron microscope (FESEM Zeiss Merlin), along with energy-dispersive X-ray spectrometer (EDX) to assess the elemental composition of the grains. The steady-state method and the conventional DC four-probe technique with an LSR-3 system (Linseis GmbH) were used to simultaneously measure the electrical resistivity and Seebeck coefficient of all samples within a temperature range of 50–800 °C under helium atmosphere. The power factor ($PF = S^2/\rho$) was subsequently calculated using the resistivity and Seebeck coefficient data to evaluate the changes in electrical performance of all samples with temperature.

3 Results and discussion

Figure 1 displays the powder X-ray diffraction (XRD) patterns for all samples within the 15–60° range for enhanced clarity. As it is evident from the plot, all diffraction peaks have been indexed to the *Pnma* space group, consistent with previously reported findings [32]. This confirms that all samples exhibit a single-phase structure and that Cr has been successfully incorporated into the manganite unit cell. To assess the impact of Cr-substitution on the lattice parameters, Eq. 1 was applied to each sample, using the *Pnma* space group established for pristine $CaMnO_3$ [32].

$$\frac{1}{d^2} = \frac{h^2+k^2}{a^2} + \frac{l^2}{c^2} \quad (1)$$

As presented in the table, the cell parameters exhibit no significant changes, apart from a slight decreasing trend. This reduction can be attributed to the marginally smaller ionic radius of Cr^{3+} (0.615 Å), compared to that of Mn^{3+} (0.645 Å) [31]. However, this decrease is very small, probably due to the substitution of a small amount of Mn^{4+} (0.53 Å) by Cr^{3+}, which would compensate the decreasing tendency of cell parameters.

The crystallite size of the synthesized $Ca_{0.99}Ce_{0.01}Mn_{1-x}Cr_xO_3$ materials ($x = 0$, 0.01, 0.03, 0.05, and 0.10) samples was estimated using the Debye–Scherrer equation from the most intense XRD peak. The equation is given by:

$$D = \frac{K\lambda}{\beta \cos\theta_\beta} \quad (2)$$

where D is the average crystallite size K is the shape factor (equal to 0.9), λ is the wavelength of the X-ray radiation used (typically Cu Kα, $\lambda = 1.5406$ Å), β is the full width at half maximum (FWHM) of the diffraction peak in radians, and θ is the Bragg angle [33]. The calculated crystallite sizes were found to be 42.04, 42.45, 43.26, 43.11, and 37.84 nm, respectively. These results indicate that low-level Cr doping ($x \leq 0.05$) slightly increases the crystallite size, suggesting improved crystallinity. However, further increasing the Cr content to $x = 0.10$ leads to a noticeable reduction in

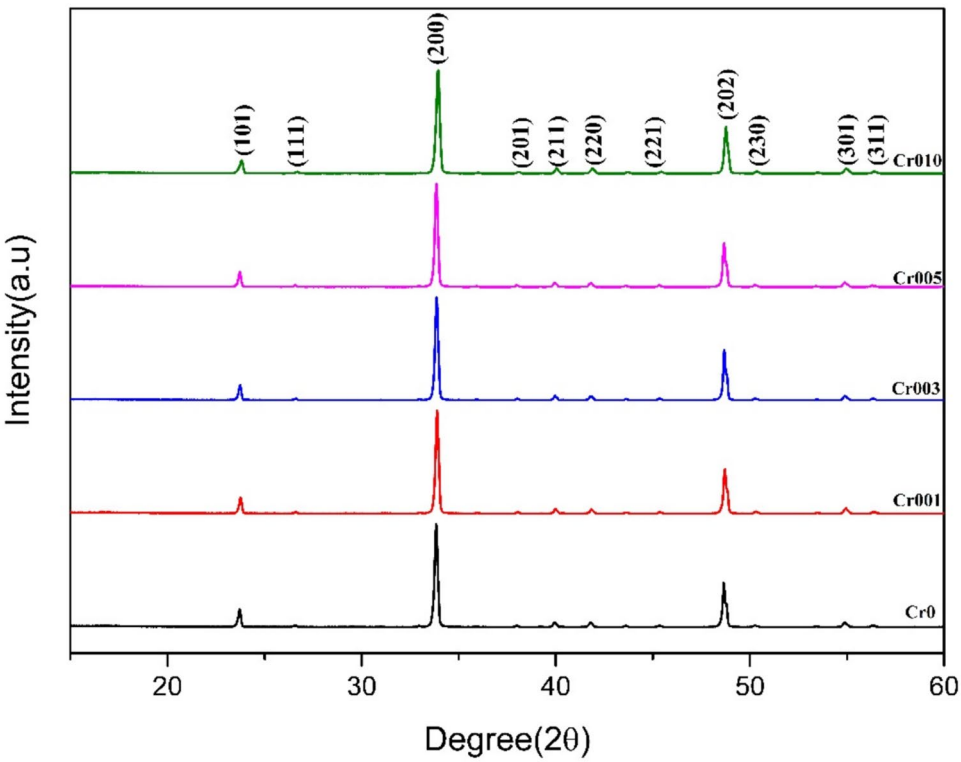

Fig. 1 Powder XRD patterns of all $Ca_{0.99}Ce_{0.01}Mn_{1-x}Cr_xO_3$ samples. The diffraction planes identify the reflections associated to the thermoelectric phase

crystallite size, which may be attributed to enhanced lattice distortion or increased defect concentration at higher doping levels, thereby hindering crystal growth. Moreover, the lattice micro-strain within the grains, denoted as ε, were determined using the Williamson-Hall (*W–H*) method [33]. This method separates the broadening of the XRD peaks into two primarily components: broadening due to crystallite size and that due to lattice strain. The total broadening (β) is expressed as a function of diffraction angle (θ) using the following equation:

$$\beta\cos\theta = \frac{k\lambda}{D} + 4\varepsilon\sin\theta \tag{3}$$

where β is the FWHM, θ is the Bragg angle, k is the shape factor (equal to 0.9), λ is the X-ray wavelength, D is the crystallite size, and ε is the micro-strain in the crystal lattice. In this method, a plot of $\beta cos\theta$ versus $4sin\theta$ yields a linear relation where the slopes correspond to the ε values. The obtained ε values are summarized in Table 1. According to the table, ε values increase progressively with Cr doping, from 1.11×10^{-3} for the undoped sample up to 1.21×10^{-3} for $x = 0.10$. This trend reflects the growing lattice distortions caused by the substitution of Cr^{3+} ions into the Mn sites. Since Cr^{3+} has a different ionic radius and electronic configuration compared to Mn^{3+} and Mn^{4+}, its incorporation disrupts the local crystal symmetry and alters the Mn–O bond lengths and angles. These distortions generate internal stresses and defects such as dislocations and oxygen vacancies, which contribute to the increased micro-strain.

Table 1 Lattice parameters, volume of the unit cell, activation energy values, average crystallite size, and microstrain values for all samples

x	a (Å)	b (Å)	c (Å)	Vol. (Å^3)	D (nm)	Microstrain (ε)×10^{-3}	E_a (meV)
0	5.306	7.499	5.322	211.76	42.04	1.15	57.9
0.01	5.297	7.496	5.317	211.12	42.45	1.12	99.8
0.03	5.296	7.492	5.311	210.72	43.26	1.04	159.4
0.05	5.291	7.486	5.304	210.08	43.11	1.07	208.5
0.10	5.287	7.476	5.301	209.47	37.84	1.17	257.6

Figure 2 presents representative SEM micrographs of the sample surfaces. An initial examination suggests that Cr doping results in a slight reduction in grain size, implying that the dopant acts as a grain growth inhibitor, which is consistent with previous observations in similar systems [34]. However, the level of porosity remains largely unchanged. Despite these microstructural variations, no secondary phases are detected, confirming the XRD findings previously discussed. Furthermore, EDS analysis performed on multiple grains from each sample confirms a chemical composition closely matching the intended stoichiometry. Additionally, doping also induces the formation of cracks in the samples, as highlighted by the arrows in the micrographs.

Figure 3 depicts the temperature-dependent electrical resistivity of all $Ca_{0.99}Ce_{0.01}Mn_{1-x}Cr_xO_3$ samples. The resistivity curves reveal a semiconducting-like behavior ($d\rho/dT < 0$) across all Cr-doped samples, whereas the undoped samples exhibit a nearly stable resistivity over the entire measured temperature range. However, all the samples display the same resistivity values between 650 and 800 ºC, while at lower temperatures; the resistivity is drastically increased when the amount of Cr is raised. This drastic increase of electrical resistivity cannot be explained by the slight decrease of grain sizes observed in the micrographs, but it can be due to the presence of cracks in the Cr-doped samples previously mentioned in the SEM discussion. The size of these cracks can be seen in Fig. 4, which presents representative overview images of the samples. As it can be clearly deduced from these micrographs, the cracks are large enough to present a serious obstacle to the charge carriers mobility, being the most important factor in the electrical resistivity values. Moreover, the amount and dimensions of cracks are increased when the Cr content is raised, explaining the electrical resistivity evolution at $T < 650$ ºC. However, the lowest measured values at 800 ºC are

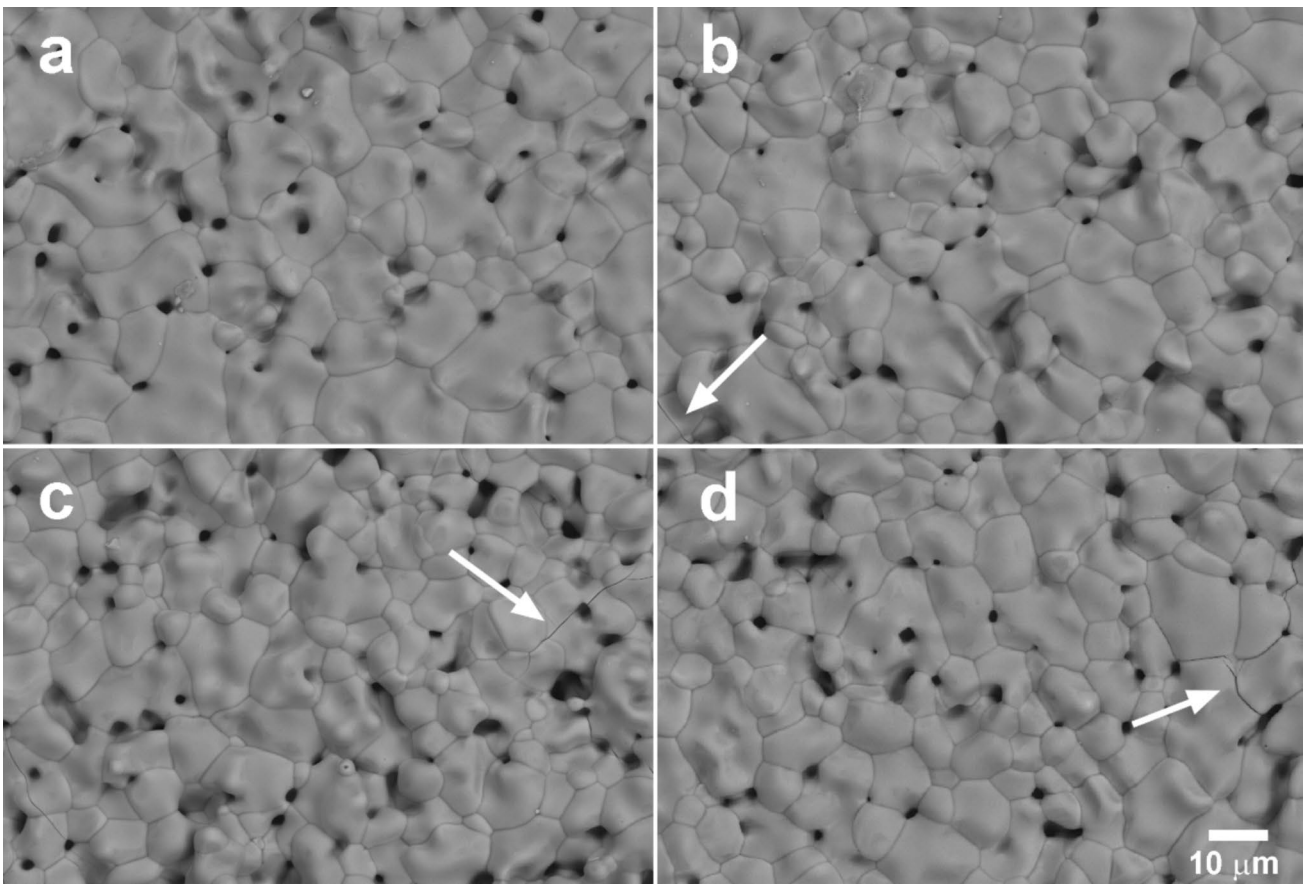

Fig. 2 Representative SEM micrographs of the surfaces of $Ca_{0.99}Ce_{0.01}Mn_{1-x}Cr_xO_3$ samples, for x = 0 **a**; 0.01 **b**; 0.05 **c**; and 0.10 **d**. The arrows show the cracks observed in the doped samples

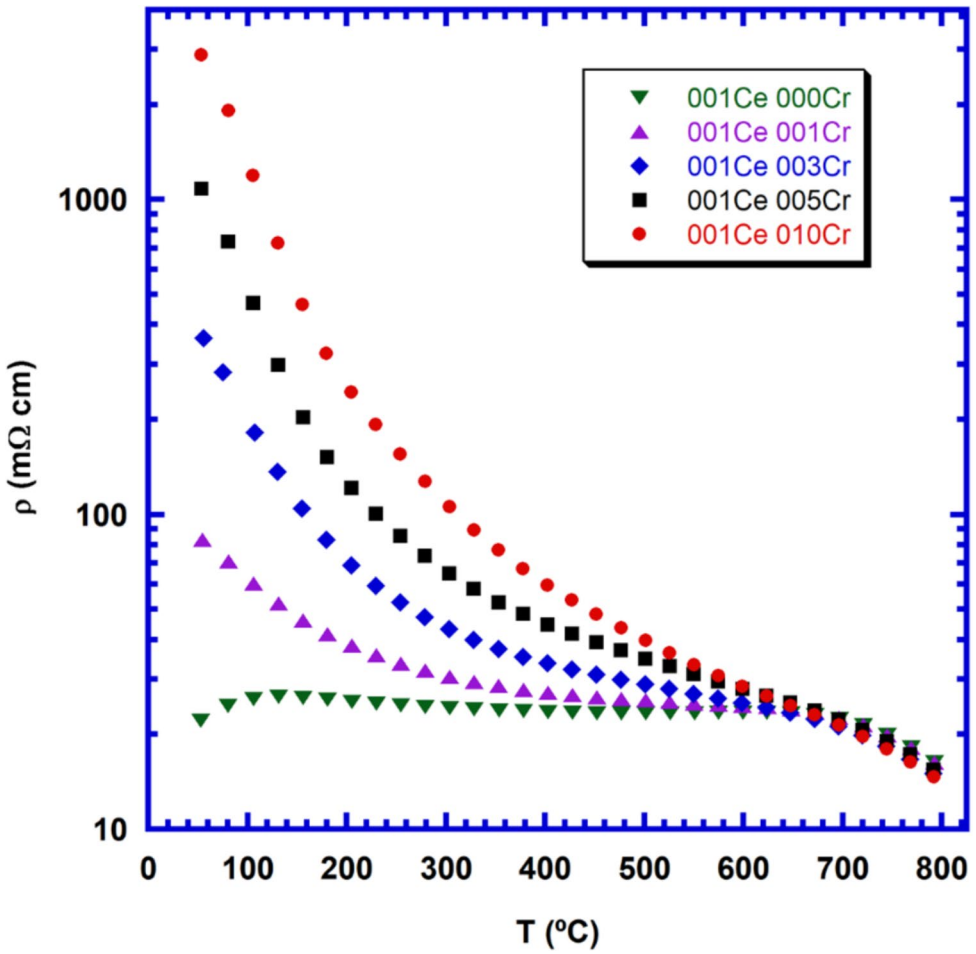

Fig. 3 Variation of electrical resistivity with temperature for all $Ca_{0.99}Ce_{0.01}Mn_{1-x}Cr_xO_3$ samples

practically the same for all samples, ~ 15.2 mΩ cm, which is considerably higher than the typical values reported in the literature for doped sintered $CaMnO_3$ materials (7–12 mΩ cm) [35–39], prepared through spark plasma sintering (SPS, 8 mΩ cm) [40], or the laser floating zone (9 mΩ cm) [41].

The charge transport mechanism in $Ca_{0.99}Ce_{0.01}Mn_{1-x}Cr_xO_3$ can be effectively interpreted through Mott's adiabatic small polaron model, where the electrical resistivity follows the expression:

$$\rho = \rho_0 T \exp\left(\frac{E_a}{k_B T}\right) \quad (3)$$

Here, ρ_0 represents the exponential factor, k_B is Boltzmann's constant, T denotes the absolute temperature, and E_a corresponds to the activation energy of the polaron carriers [42]. E_a is extracted from the linear fits of $ln\rho/T$ against $1000\ T^{-1}$, as depicted in Fig. 5. The linearity of these graphs validates the model's effectiveness in explaining the conduction mechanisms in the system. Moreover, calculated E_a values for the samples, as listed in Table 1, exhibit a consistent increase with the addition of Cr. It can be said that the incorporation of Cr^{3+} ions introduces localized electronic states and lattice disorder, which increase the potential energy barrier for carrier transport. In addition, microstructural features such as grain boundary cracks, which are more prevalent in Cr-doped samples, act as scattering centers and trap sites that further hinder polaron mobility. Consequently, the elevated energy barrier impedes polaron hopping and leads to higher electrical resistivity.

Figure 6 illustrates the temperature dependence of the Seebeck coefficient for all compositions. Across the entire measured temperature range, the coefficient remains negative, indicating an n-type conduction mechanism governed by electron transport. On the other hand, at low temperatures, |S| increases with rising temperature before reaching a maximum and subsequently declining at higher temperatures. The temperature where the maximum |S| is obtained

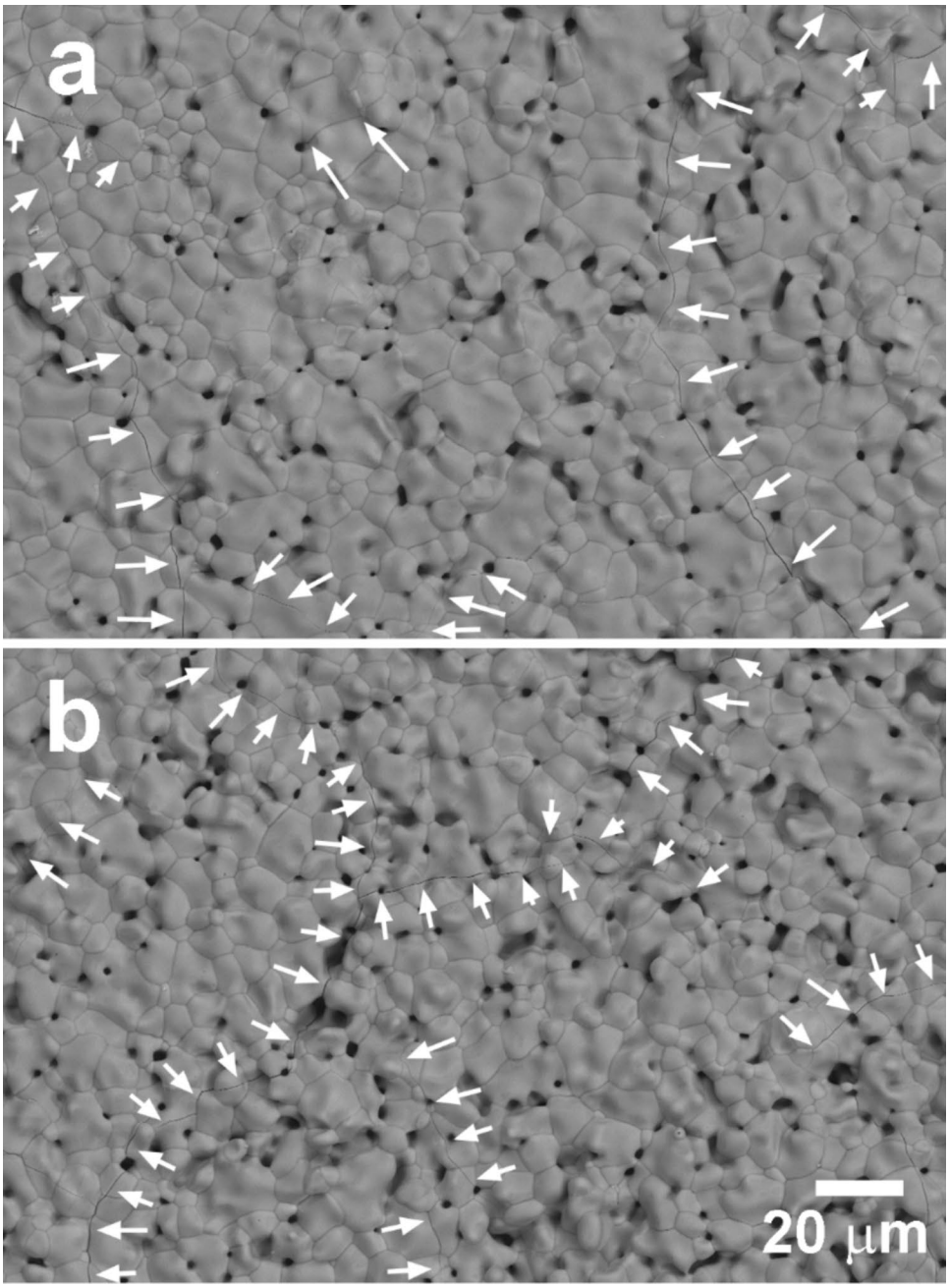

Fig. 4 Representative general SEM micrographs of the surfaces of $Ca_{0.99}Ce_{0.01}Mn_{1-x}Cr_xO_3$ samples, for x = 0.01 **a**; and 0.05 **b**. The arrows show the beginning and the end of some cracks

is increased when the Cr amount is increased up to 0.05, decreasing for higher Cr content. Moreover, at room temperature, |S| values increase with the Cr addition, reflecting the effect of cracks in the samples. These microstructural defects, such as cracks, can act as energy-dependent scattering centers that preferentially scatter low-energy carriers, effectively enhancing the average energy of the charge carriers contributing to conduction and thereby increasing |S|.

Nevertheless, the S curves evolution with temperature displays some crossovers, and the highest |S| value at 800 ºC is achieved for the 0.03Cr-substituted sample (230 μV/K), which is much higher than the reported in sintered materials (140–160 μV/K) [35–39], prepared using SPS (145 μV/K) [40], or laser grown materials (190 μV/K) [41]. This remarkable enhancement in |S| at high temperature suggests that careful tuning of Cr doping optimizes the balance between

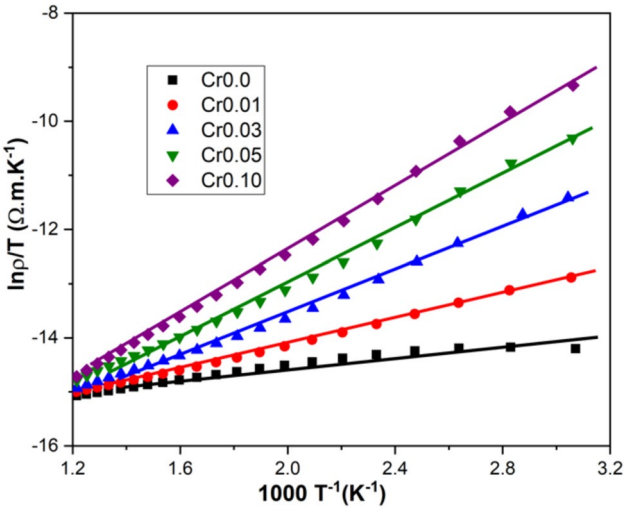

Fig. 5 The plots of lnρ/T versus 1000 T^{-1} for the samples

carrier concentration and scattering mechanisms, improving the thermoelectric power.

The temperature-dependent power factor (PF), calculated from the Seebeck coefficient and resistivity measurements, is shown in Fig. 7. As evident from the graph, at room temperature PF decreases when the amount of Cr is increased, reflecting the large contribution of electrical resistivity to these PF values. On the other hand, the large decrease in resistivity with temperature for all doped samples increases the Seebeck contribution, and PF at 800 ºC is increased with Cr-concentration up to 0.03, decreasing for further substitution. The peak values at 800 ºC for the 0.03Cr-doped samples (~ 0.35 mW/K^2m) exceed those reported for sintered samples (0.10–0.25 mW/K^2m) [35, 37, 38] and those fabricated using SPS (0.26 mW/K^2m) [40]. However, they are in the order of the reported results for co-doped materials (0.095–0.35 mW/K^2m) [43–45], or laser grown samples (0.39 mW/K^2m) [41]. On the other hand, it presents higher values than the obtained in GeSn manowires (0.24 mW/K^2m) [46, 47],

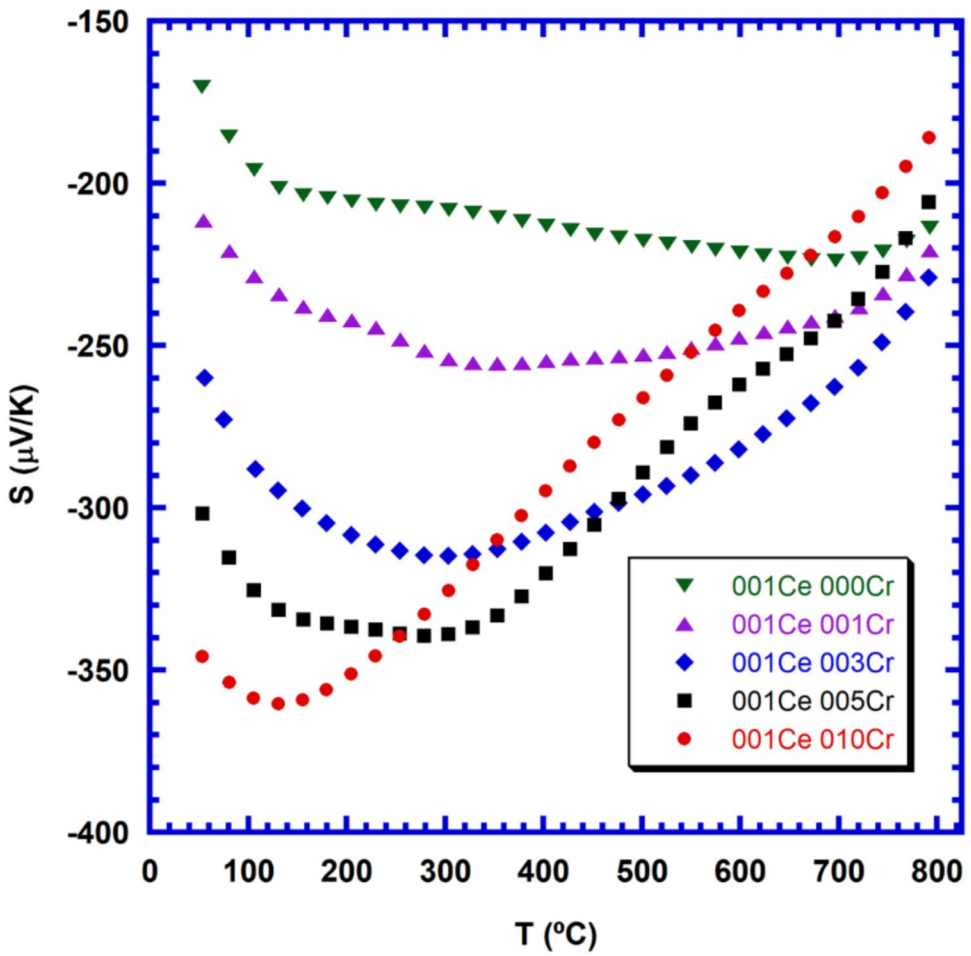

Fig. 6 Variation of Seebeck coefficient with temperature for all $Ca_{0.99}Ce_{0.01}Mn_{1-x}Cr_xO_3$ samples

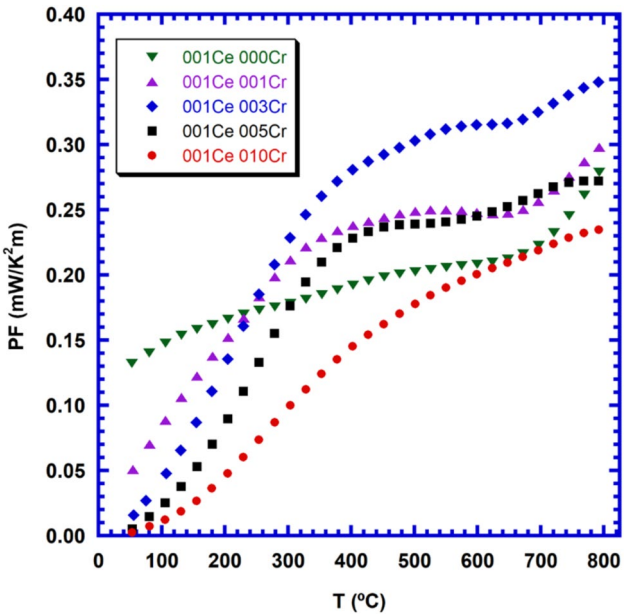

Fig. 7 Variation of power factor with temperature for all $Ca_{0.99}Ce_{0.01}Mn_{1-x}Cr_xO_3$ samples

and much lower than those obtained in SiGe nanomaterials (4 mW/K^{2}m) [48]. Nevertheless, the results obtained in this study are obtained using much cheaper precursors than Ge, combined with a simple and scalable synthesis approach, eliminating the need for complex or time-consuming fabrication processes. Furthermore, the dopant cations have been chosen being more abundant and with lower costs than the typically used in literature.

4 Conclusion

In this study, Ce–Cr substituted $Ca_{0.99}Ce_{0.01}Mn_{1-x}Cr_xO_3$ samples ($x = 0$, 0.01, 0.03, 0.05, and 0.10) were synthesized using the well-known solid-state technique. XRD analysis confirmed the successful incorporation of Cr into the orthorhombic *Pnma* structure without the formation of secondary phases. Moreover, a slight decrease in lattice parameters was observed due to the smaller ionic radius of Cr^{3+} compared to Mn^{3+}. FESEM observation revealed that Cr doping inhibits grain growth and induces crack formation. These cracks were identified as the primary factor contributing to the significant increase in electrical resistivity at low temperatures, as they hinder charge carrier mobility. The charge transport mechanism was effectively described by Mott's adiabatic small polaron model, with activation energy increasing with Cr content. The Seebeck coefficient confirmed n-type conduction, and the highest power factor (~0.35 mW/K^{2}m) was achieved for the 0.03Cr-doped sample at 800 °C, outperforming many reported values for sintered and laser-grown materials. This study demonstrates that Cr-doped $Ca_{0.99}Ce_{0.01}MnO_3$, synthesized via a simple and scalable method, offers a promising route for developing cost-effective thermoelectric materials with competitive performance.

Acknowledgements

This work was supported by Çukurova University Scientific Research Projects, Adana, Turkey, under grant contracts no FBA-2024-16531 and FYL-2024-16801. M. A. Torres, M. A. Madre and A. Sotelo wish to thank the Gobierno de Aragón (Grupo de Investigacion T54_23R) for financial support. Authors would like to acknowledge the use of Servicio General de Apoyo a la Investigación-SAI, Universidad de Zaragoza.

Author contributions

L. KORKMAZ: Material preparation, Data curation, Formal Analysis. C. ÖZÇELİK: Material preparation, Data curation, Formal Analysis. M. GÜRSUL: Data curation, Visualization, Writing—Review & Editing. M.A. TORRES: Data curation, Formal analysis, Software. M.A. MADRE: Data curation, Formal analysis, Writing—Review & Editing. A. SOTELO: Project Administration, Writing—Review & Editing. B. ÖZÇELİK: Project Administration, Writing—Review & Editing.

Funding

Open access funding provided by the Scientific and Technological Research Council of Türkiye (TÜBİTAK).

Data availability

Data will be made available on reasonable request.

Declarations

Conflict of interest The author declares no competing interests.

Ethical approval Approval not applicable.

Consent for publication Not applicable.

References

1. S. Sorrell, Reducing energy demand: a review of issues, challenges and approaches. Renew. Sust. Energ. Rev. **47**, 74–82 (2015)
2. S. Chu, Y. Cui, N. Liu, The path towards sustainable energy. Nat. Mater. **16**, 16–22 (2017)
3. D.M. Rowe, Review, THERMOELECTRIC WASTE HEAT RECOVERY AS A RENEWABLE ENERGY SOURCe. Int. J. Innov. Energy Systems Power **1**, 13–23 (2006)
4. D. Zhao, G. Tan, A review of thermoelectric cooling: materials, modeling and applications. App. Thermal Eng. **66**, 15–24 (2014)
5. G.J. Snyder, Small thermoelectric generators. Interface **17**, 54–56 (2008)
6. L.E. Bell, Cooling, heating, generating power, and recovering waste heat with thermoelectric systems. Science **321**, 1457–1461 (2008)
7. G.J. Snyder, E.S. Toberer, Complex thermoelectric materials. Nat. Mater. **7**, 105 (2008)
8. C. Wood, Materials for thermoelectric energy conversion. Rep. Prog. Phys. **51**, 459 (1988)
9. Y. Wang, Y. Sui, H. Fan, X. Wang, Y. Su, W. Su, X. Liu, High temperature thermoelectric response of electron-doped $CaMnO_3$. Chem. Mater. **21**, 4653–4660 (2009)
10. Z. Kong, G. Wang, R. Liang, J. Su, M. Xun, Y. Miao, S. Gu, J. Li, K. Cao, H. Lin, B. Li, Y. Ren, J. Li, J. Xu, H.H. Radamson, Growth and strain modulation of GeSn alloys for photonic and electronic applications. Nanomaterials **12**, 981 (2022)
11. J. Yang, H. Hu, Y. Miao, B. Wang, W. Wang, H. Su, Y. Ma, Single-crystalline GePb alloys formed by rapid thermal annealing-induced epitaxy. J. Phys. D Appl. Phys. **53**, 265105 (2020)
12. H. Wang, J. Hwang, M.L. Snedaker, I.-H. Kim, C. Kang, J. Kim, G.D. Stucky, J. Bowers, W. Kim, High thermoelectric performance of a heterogeneous PbTe nanocomposite. Chem. Mater. **27**, 944–949 (2015)
13. T. Wang, P. Nan, H.C. Wang, W. Su, A. Sotelo, J. Zhai, X. Wang, Y. Ran, T. Chen, C.L. Wang, Right heterogeneous microstructure for achieving excellent thermoelectric performance in $Ca_{0.9}R_{0.1}$MnO3-δ (R=Dy, Yb) ceramics. Inorg. Chem. **57**, 9133–9141 (2018)
14. A.A. Yaroshevsky, Abundances of chemical elements in the earth's crust. Geochem. Int. **44**, 48–55 (2006)
15. S. LeBlanc, Thermoelectric generators: linking material properties and systems engineering for waste heat recovery applications. Sust. Mater. Technol. **1–2**, 26–35 (2014)
16. J. He, Y. Liu, R. Funahashi, Oxide thermoelectrics: the challenges, progress, and outlook. J. Mater. Res. **26**, 1762–1772 (2011)
17. H. Wang, W. Su, J. Liu, C. Wang, Recent development of n-type perovskite thermoelectrics. J. Materiomics **2**, 225–236 (2016)
18. L. Bocher, M. Aguirre, D. Logvinovich, A. Shkabko, R. Robert, M. Trottmann, A. Weidenkaff, $CaMn_{1-x}Nb_xO_3$ ($x \leq 0.08$) perovskite-type phases as promising new high-temperature n-type thermoelectric materials. Inorg. Chem. **47**, 8077–8085 (2008)
19. M. Ohtaki, H. Koga, T. Tokunaga, K. Eguchi, H. Arai, Electrical transport properties and high-temperature thermoelectric performance of $Ca_{0.9}M_{0.1}MnO_3$ (M= Y, La, Ce, Sm, In, Sn, Sb, Pb, Bi). J. Solid State Chem. **120**, 105–111 (1995)
20. T. Kobayashi, H. Takizawa, T. Endo, T. Sato, M. Shimada, H. Taguchi, M. Nagao, Metal-insulator transition, and thermoelectric properties in the system $(R_{1-x}Ca_x)$ $MnO_{3-\delta}$ (R: Tb, Ho, Y). J. Solid State Chem. **92**, 116–129 (1991)
21. M. Gürsul, G. Çetin, İ Ergin, L. Korkmaz, B. Özçelik, M.A. Torres, M.A. Madre, A. Sotelo, Remarkable variation in

microstructural, thermoelectric, and magnetic properties of $CaMnO_3$ through Ce doping. Mater. Sci. Eng. B **299**, 116986 (2024)
22. P. Amirkhizi et al., Effect of B-site doping on the thermoelectric performances of $Ca_{0.97}Y_{0.01}La_{0.01}Yb_{0.01}Mn_{1-2x}Nb_xMo_xO_3$ thermoelectric ceramics. J. Eur. Ceram. Soc. **44**, 2982–2988 (2024)
23. A. Sotelo, P. Amirkhizi, O.J. Dura, G. Garcia, A.C. Asemsio, M.A. Torres, M.A. Madre, A. Kovalevsky, Sh. Rasekh, Significant reduction in processing time for $Ca_{0.95}Ce_{0.05}MnO_3$ thermoelectric ceramics. Ceram. Int. **49**, 37793–37799 (2023)
24. Y. Zhu, C. Wang, W. Su, J. Liu, J. Li, X. Zhang, L. Mei, Influence of rare-earth elements doping on thermoelectric properties of $Ca_{0.98}Dy_{0.02}MnO_3$ at high temperature. J. Solid State Chem. **225**, 105–109 (2015)
25. F.P. Zhang, Q.M. Lu, X. Zhang, J.X. Zhang, Preparation and improved electrical performance of the Pr-doped $CaMnO_{3-\delta}$ thermoelectric compound. Phys. Scr. **88**, 035705 (2013)
26. J.B. MacChesney, H.J. Williams, J.F. Potter, R.C. Sherwood, Magnetic study of the manganate phases: $CaMnO_3$, $Ca_4Mn_3O_{10}$, $Ca_3Mn_2O_7$, Ca_2MnO_4. Phys. Rev. **164**, 779 (1967)
27. N. Sharma, A. Das, C.L. Prajapat, A. Kumar, M.R. Singh, Phase separated behavior in yttrium doped $CaMnO_3$. Mater. Res. Bull. **77**, 284–290 (2016)
28. R. Bharamagoudar et al., Low temperature magnetic properties of Gd doped $CaMnO_3$. Chem. Data Collec. **39**, 100846 (2022)
29. A. Mishra, S. Bhattacharjee, Effect of A- or B-site doping of perovskite calcium manganite on structure, resistivity, and thermoelectric properties. J. Am. Ceram. Soc. **100**, 4945–4953 (2017)
30. R. Bharamagoudar, V.J. Angadi, I. Shivaraja, B. Angadi, R. Mondal, A.S. Patil, S. Patil, V. Pattar, S. Raghu, S. Matteppanavar, Evidence of weak ferromagnetism, space charge polarization, and metal to insulator transition in Dy-Doped $CaMnO_3$. J. Supercond. Nov. Magn. **34**, 837–844 (2021)
31. http://abulafia.mt.ic.ac.uk/shannon/ptable.php
32. K.R. Poeppelmeier, M.E. Leonowicz, J.C. Scanlon, J.M. Longo, W.B. Yelon, Structure determination of $CaMnO_3$ and $CaMnO_{2.5}$ by X-ray and neutron methods. J. Solid State Chem. **45**, 71–79 (1982)
33. Radamson, H.H. (2023). X-Ray Techniques. In: Analytical Methods and Instruments for Micro- and Nanomaterials. Lecture Notes in Nanoscale Science and Technology, vol 23. Springer, Cham. https://doi.org/10.1007/978-3-031-26434-4_1
34. M.A. Madre, H. Amaveda, O.J. Dura, D. Pelloquin, M. Mora, M.A. Torres, S. Marinel, A. Sotelo, Effect of Y, La, and Yb simultaneous doping on the thermal conductivity and thermoelectric performances of $CaMnO_3$ ceramics. J. Alloy. Compd. **954**, 170201 (2023)
35. D. Flahaut, T. Mihara, R. Funahashi, N. Nabeshima, K. Lee, H. Ohta, K. Koumoto, Thermoelectrical properties of A-site substituted Ca1−xRexMnO3 system. J. Appl. Phys. **100**, 084911 (2006)
36. Y. Wang, Y. Sui, J. Cheng, X. Wang, Z. Lu, W. Su, High temperature metal-insulator transition induced by rare-earth doping in perovskite $CaMnO_3$. J. Phys. Chem. C **113**, 12509–12516 (2009)
37. R. Kabir, D. Wang, T. Zhang, R. Tian, R. Donelson, T.T. Tan, S. Li, Tunable thermoelectric properties of $Ca_{0.9}Yb_{0.1}MnO_3$ through controlling the particle size via ball mill processing. Ceram. Int. **40**, 16701–16706 (2014)
38. Y.C. Zhou, C.L. Wang, W.B. Su, J. Liu, H.C. Wang, J.C. Li, Y. Li, J.Z. Zhai, Y.C. Zhang, L.M. Mei, Electrical properties of Dy^{3+}/Na^+ Co-doped oxide thermoelectric $[Ca_{1-x}(Na_{1/2}Dy_{1/2})_x]MnO_3$ ceramics. J. Alloy. Compd. **680**, 129–132 (2016)
39. Y.-H. Zhu, W.-B. Su, J. Liu, Y.-C. Zhou, J. Li, X. Zhang, Y. Du, C.-L. Wang, Effects of Dy and Yb co-doping on thermoelectric properties of $CaMnO_3$ ceramics. Ceram. Int. **41**, 1535–1539 (2015)
40. S. Quetel-Weben, R. Retoux, J.G. Noudem, Thermoelectric $Ca_{0.9}Yb_{0.1}MnO_{3-\delta}$ grain growth controlled by spark plasma sintering. J. Eur. Ceram. Soc. **33**, 1755–1762 (2013)
41. N.M. Ferreira, N.R. Neves, M.C. Ferro, M.A. Torres, M.A. Madre, F.M. Costa, A. Sotelo, A.V. Kovalevsky, Growth rate effects on the thermoelectric performance of $CaMnO_3$-based ceramics. J. Eur. Ceram. Soc. **39**, 4184–4188 (2019)
42. K.K. Liu, Z.Y. Liu, F.P. Zhang, J.X. Zhang, X.Y. Yang, J.W. Zhang, J.L. Shi, G. Ren, T.W. He, J.J. Duan, Improved thermoelectric performance in Pr and Sr Co-doped $CaMnO_3$ materials. J. Alloy. Compd. **808**, 151476 (2019)
43. B. Zhang, A. Chang, Q. Zhao, H. Ye, Y. Wu, Synthesis and thermoelectric properties of Yb-doped $Ca_{0.9-x}Yb_xLa_{0.1}MnO_3$ ceramics. J. Electron. Mater. **43**, 4048–4055 (2014)
44. H. Wang, C. Wang, Synthesis of Dy doped $Yb_{0.1}Ca_{0.9}MnO_3$ ceramics with a high relative density and their thermoelectric properties. Mater. Res. Bull. **47**, 2252–2256 (2012)
45. Y. Zhu, C. Wang, H. Wang, W. Su, J. Liu, J. Li, Influence of Dy/Bi dual doping on thermoelectric performance of $CaMnO_3$ ceramics. Mater. Chem. Phys. **144**, 385–389 (2014)

46. M. Noroozia, B. Hamawandia, M. S. Topraka, H. H. Radamson, Fabrication and thermoelectric characterization of GeSn nanowires, 15th International Conference on Ultimate Integration on Silicon (New York, NY: IEEE) (2014) 125–128.
47. Y. Li, G. Wang, M. Akbari-Saatlu, M. Procek, H.H. Radamson, Si and SiGe nanowire for micro-thermoelectric generator: a review of the current state of the art. Frontiers Mater. **8**, 611078 (2021)
48. B. Yu, M. Zebarjadi, H. Wang, K. Lukas, H. Wang, D. Wang, C. Opeil, M. Dresselhaus, G. Chen, Z. Ren, Enhancement of Thermoelectric properties by modulation-doping in silicon germanium alloy nanocomposites. Nano Lett. **12**, 2077–2082 (2012)